RSC Advances

ROYAL SOCIETY OF CHEMISTRY

www.rsc.org/advances

Graphene oxide incorporated TiO₂ photoanode for high efficiency quasi solid state dye sensitized solar cells based on poly-vinyl alcohol gel electrolyte

MominaKhannam,[a] Shyamalima Sharma, [a] Swapnil Dolui, [a] Swapan Kumar Dolui,[a],*

[a]Department of Chemical Sciences, Tezpur University, Napaam, Sonitpur, Assam-784028, India

*Author for correspondence: S.K. Dolui, Department of Chemical Sciences, Tezpur University, Napaam, Tezpur, Dist. Sonitpur, Assam, India. Tel No: 9957198489. Email: dolui@tezu.ernet.in

Abstract

An effective self assembly method was used to synthesize hybrid nanocomposites of TiO₂ nanoparticles on graphene oxide (GO) sheets for application in Dye Sensitized Solar Cells (DSSCs). The successful incorporation of TiO₂ on the GO sheets was confirmed by X-ray diffraction (XRD), Energy Dispersive X-ray spectrum (EDX) Raman and UV-Visible spectroscopy. The morphology and size of the TiO₂ nanoparticles on the GO sheets were analyzed by scanning electron microscope (SEM) and transmission electron microscopic (TEM) analysis. This manuscript is concerned with the effects of different GO contents of the photoanode on the energy conversion efficiency of the PVA gel electrolyte based DSSCs. DSSCs based on GO@TiO₂ nanocomposite photoanode with an optimum concentration of GO content of 2.5 wt% showed a short circuit current density (J_{sc}) of 7.67mAcm^{-2}, an open circuit voltage (V_{oc}) of 0.76V and photo conversion efficiency of 3.97% which is much higher than that of the pure TiO₂ nanoparticles.

Key words: Nanocomposites; Dye sensitizedsolar cells; GO; PCE

1. Introduction

Dye sensitized solar cell is the mostly studied device of the last two decades as the most promising alternatives to the silicon solar cells because of its low cost, facile fabrication process and high efficiency.[1,2] In 1991, Grätzel and O'regan assembled and demonstrated the first dye sensitized solar cell consisting of a photoanode of transparent fluorine doped tin oxide glass (FTO), a wide band gap nanocrystalline n-type semiconductor, a visible-light absorber, a redox couple electrolyte and a counter electrode of platinum. The performance of photoelectric conversion of DSSCs depends on the four key factors: abundant photoelectron generation by dyes, rapid electron transfer at the photoanode, fast ion diffusion in the electrolyte and efficient reduction of redox media at the counter electrode. Amongst all components in DSSC, the photoanode material plays a very important role in the dye loading, electron injection, transportation and collection, in turn significantly influences the photoconversion efficiency.[3-6]

The photoanode of DSSCs is made of nanoparticles, which was sintered into a mesoporous network on FTO. Electron transports in the disordered TiO_2 nanoparticles with a random motion resulting in the possibility of charge recombination and thus reduces the photocurrent and the performance of the device. [7,8] Therefore, in order to improve the performance of DSSCs designing of photoanode in a manner is very important so that photogenerated electrons can be transported across the TiO_2 nanoparticle network, competing with the charge recombination.[9-11] The choice of photoanode material is based on two main factors: energy gap of the semiconductor must match with that of the dye so that photo-generated electrons can easily transfer from dyes to semiconductor. Secondly, to harvest solar energy as much as possible, semiconductor must have a high surface area so that more dye molecules get adsorbed on it. To enhance the electron transport and to reduce the recombination, there are several kinds of photoanode materials that have been developed including doped TiO_2,[12,13] metal/metal oxide−TiO_2 hybrid, composite and core−shell structures,[14-16] porous TiO_2 structures,[17-21] and TiO_2−carbon material. [22-24]

Now a days, the 2D carbon nanomaterial graphene has drawn much attention as it is a zero band gap material resulting in an excellent electrical conduction in two dimensions. Herein, we incorporate graphene oxide (GO) into TiO_2 nanoparticles (GO@TiO_2) so that GO can form some bridges and enhance the charge transport rate to prevent the charge recombination

improving photoelectrical conversion efficiency. TiO_2 nanoparticles are anchored compactly on the GO flakes through physisorption, electrostatic binding or charge transfer interaction. As GO is an excellent electrical conductor it behaves as an electron transfer medium to enhance the electron transport from conduction band of TiO_2 and resulting in the reduced recombination. [25] In DSSCs, triodide / iodide (I_3^-/I^-) is used as redox couple electrolyte. The volatile nature of different organic solvents used in liquid electrolytes triggers leakage and evaporation thus restricting long term performance of DSSCs. To overcome these drawbacks people focused on alternatives to the liquid electrolyte. In recent times, polymer gel electrolyte offers a great area of research as it possess the properties of solid as well as liquid and the unique hybrid network structure results in lower leakage and evaporation with long term durability of the cell. The effect of such electrolyte in GO@TiO_2 photoanode based DSSCs are yet to be studied. Inspired from the forgoing discussions, a series of quasi solid state DSSCs have been fabricated using different weight% of GO@TiO_2 photoanode and an attempt has been made to replace the conventional liquid electrolyte with a PVA gel electrolyte. Among the various polymers poly (vinyl alcohol) (PVA) has been chosen because of its good film forming properties and physical properties, biocompatibility, and have good chemical resistance.

Experimental

Materials and methods

2.1   Materials

Poly (vinyl alcohol), gluteraldehyde, nitric acid (HNO_3), lithium iodide (LiI), and iodine (I_2) were purchased from Merck India. The chemicals tertiary butylpyridine (TBP), 1-methyl-3propyl imidazolium iodide (MPI), N-methyl 2-pyrrolidone (NMP), Cis-bis(isothiocyanato)bis(2,2$^{/}$-bipyridyl-4,4$^{/}$-dicarboxylato)   ruthenium(II)bis-tetrabutylammonium (N719) dye, acetonitrile, fluorine doped tin oxide (FTO) coated glasses (Sheet resistance: 15Ω/sq) were purchased from Sigma Aldrich India.

Sodium   nitrate   ($NaNO_3$),   potassium   permanganate   ($KMnO_4$),   sodium   dodecyl sulfate($CH_3(CH_2)_{11}OSO_3Na$) (Merck), $TiCl_3$ (Merck), Sodium sulfate (Na_2SO_4), Hydrogen peroxide (H_2O_2) were purchased from Merck India. Graphite powder (<20 μm, Sigma-Aldrich; 99% pure) were used without further purification.

2.2   Preparation of TiO$_2$@ GO nanocomposite:

2.2.1 Synthesis of Graphene oxide

Graphene oxide was synthesized from natural graphite powder by using Hummers method. [26] Graphite (5 g), $NaNO_3$ (2.5 g) and H_2SO_4 (120 mL) were mixed in a 500 mL beaker and the mixture was stirred vigorously in an ice bath for 30 min. Under constant stirring 15 g of $KMnO_4$ was added to the above suspension in a very controlled way so that the reaction temperature remains below 20°C. The mixture was kept under stirring for 12 h at room temperature, followed by the addition of 150 mL of distilled water and kept for 24 h under constant stirring. Then 50 mL of 30% H_2O_2 was added to the mixture and stirred for another 6 h. Finally, the obtained product was washed with 5% HCl and followed by distilled water so that the pH of the filtrate becomes 7 and dried in vacuum oven. The obtained graphene oxide was then dispersed and exfoliated in deionized water by using an ultrasonic bath for 40 min. The obtained graphene oxide suspension was then used for the synthesis of $GO@TiO_2$ nanocomposites.

2.2.2 Synthesis of $GO@TiO_2$ nanocomposite

$GO@TiO_2$ nanocomposites were synthesized by a previously reported self-assembly method.[27] The GO suspension (1.3 gL^{-1}) was made with the addition of sodium dodecyl sulfate. To this mixture an aqueous solution of 50ml of 0.12 mol L^{-1} $TiCl_3$ was added and kept for 1 h under constant stirring. To the mixture, 10ml of 0.6 M Na_2SO_4 solution and 5 mL of 1 wt % H_2O_2 solution were added and stirring was continued for another 1 h at 90 °C. The final precipitates of the reactions were separated and washed with water and ethanol and then dried at 70 °C. Finally, the dried product was calcinated at 400 °C for 2 h. Five sets of $GO@TiO_2$ nanocomposites viz. *$GO@TiO_2$-A*, *$GO@TiO_2$-B*, *$GO@TiO_2$-C*, *$GO@TiO_2$-D* & *$GO@TiO_2$-E* having GO wt% of 0.25, 0.5, 1, 2.5 & 5 respectively were synthesized by taking different amounts of GO. The compositions of the prepared $GO@TiO_2$ nanocomposites are given in **Table 1**.

2. 3 Synthesis of PVA hydrogel

PVA hydrogel was prepared by dissolving 1g of PVA polymer powder in 10mL of deionized water and kept under constant stirring at a temperature of 80°C until the PVA is completely soluble. The PVA solution was allowed to cool down to room temperature, then

chemically cross linked by adding 1.5mL of   glutaraldehyde and allowed to form gel at 60-70 °C. [28] The obtained PVA hydrogel was then washed thoroughly and dried in a vacuum oven at 60°C. The product was collected for further analysis and applications.

2. 4   Preparation of PVA gel electrolyte:

The gel electrolyte was prepared by dipping 0.5 g of dried PVA hydrogel in liquid electrolyte for about 48 hrs so that the gels reach equilibrium absorption. The liquid electrolyte consists of 0.1 M lithium iodide (LiI), 0.6 M I_2, 0.5 M tertiarybutylpyridine (TBP), 0.05 M 1-methyl-3propyl imidazolium iodide (MPI) in a mixed solvent of N-methyl 2-pyrrolidone (NMP) and acetonitrile 2:8 ration.

2.5   Assembling of Dye Sensitized Solar Cell

FTO glass sheets (Sigma-Aldrich, sheet resistance: 15Ω/sq) were first cleaned by ultrasonicating in a detergent and deionized water followed by treating with boiling acetone and isopropanol and fiinally dried under a nitrogen atmosphere. Then $GO@TiO_2$ nanocomposites photoanode electrodes were prepared by depositing a paste of $GO@TiO_2$ nanocomposites on FTO by doctor blade technique, which was annealed at 450^0C for 30 minutes to retain the texture. Finally the annealed photoanodes were sensitized by immersing into a 0.3 mM N719 dye solution prepared in a mixed solvent of acetonitrile and ethanol with a volume ratio of 1:1 for 24 h. After that the elecrodes were washed properly with ethanol and dried in air before the final assembling of the devices. The platinum deposited FTO coated glass slide was used as the counter electrode. DSSCs was fabricated by placing the PVA gel electrolyte evenly in between the dye adsorbed photoanodes and Pt counter electrode. Before taking the photovoltaic measurements, all the devices were kept at 70 °C for 10 min so that the electrolyte can penetrate into dye adsorbed $GO@TiO_2$ nanocomposites layer. A schematic presentation of the structure of quasi solid state DSSC is shown in Fig. 1.

2.6   Measurements

2.6.1   *X-ray diffractometer (XRD):*

The XRD measurements were carried out in a Rigaku X-ray diffractometer (Miniflex, UK) using CuKα (λ=0.154 nm) radiation at a scanning rate of 2° min^{-1} with an angle (2θ) ranging from 10° to 80° to study the structural characteristics of the synthesized nanocomposites.

2.6.2   *Ultraviolet-visible (UV-vis) spectroscopy:*

The optical property of MWCNT@TiO$_2$ nanocomposites were measured by using UV-Visible diffuse reflectance spectra in the range 200–800 nm using Shimadzu UV-2550 UV-visible spectrophotometer.

2.6.3   *Scanning Electron Microscopy (SEM):*

The surface morphologies of the prepared samples were studied by using a Jeol-JSM-6390L V scanning electron microscope at an accelerating voltage of 5-15kV. The surface of the samples was Pt-coated before the scanning.

2.6.4   *Transmission electron microscopy (TEM):*

To study the distribution of the of particles within the nanocomposites, TEM analysis was done in a JEOL, JEM 2100 transmission electron microscope at an accelerating voltage of 200 kV.

2.6.5   *Impedance spectroscopy measurement of devices:*

The impedance spectroscopy was performed on a SP-150 Potentiostat Galvanostat electrochemical impedance workstation at a constant temperature of 25^{0}C. The amplitude of the applied ac signal was of 90 to 264 V in the frequency range from 100 mHz to 100 kHz.

2.6.6   *Photovoltaic Test*

The photocurrent voltage characteristic curves of the fabricated gel electrolyte based DSSCs was measured using a 100 mW cm^{-2} xenon arc lamp in ambient atmosphere. The performance parameters of the fabricated devices i.e. the cell fill factor (FF) and cell power conversion efficiency (Ƞ) were calculated by following Eqn. 1 and Eqn. 2 respectively.

$$FF = \frac{J_{max} \times V_{max}}{J_{sc} \times V_{oc}}$$ Eqn. 1

$$\eta(\%) = \frac{FF \times J_{sc} \times V_{oc}}{P_{in}} \times 100 \qquad\qquad \text{Eqn. 2}$$

Where, J_{max} and V_{max} are the maximum current density and voltage respectively, at the point of maximum power of photocurrent density versus voltage plot. J_{sc} is the short circuit current density (mA cm^{-2}), V_{oc} is the open circuit voltage (V) and P_{in} is the intensity of the incident white light.

3. Results and discussion

3.1   *Ultraviolet-visible (UV-vis) spectroscopy*

UV-Visible analysis is recorded in the range of 200-800nm and the spectra of GO@TiO$_2$ nanocomposites are shown in **Fig.2(a).** The presence of different amounts of GO influences the optical absorption for GO@TiO$_2$ nanocomposites significantly. All the nanocomposites show the same absorption profile. However with increasing GO content in the nanocomposite absorption intensity in the UV region raises.[29] A red shift to higher wavelength in the absorption edge of the GO@TiO$_2$ nanocomposites has also been observed at about 400nm, indicating a narrowing of the band gap of TiO$_2$. Due to the incorporation of GO into the matrix of TiO$_2$, the background absorption in the area 400-800nm increases resulting in the difficulty to measure the red shift.

Optical band gap calculations are carried out using the Tauc's relationship. The Tauc's equation for band gap calculations is described as,

$$(\alpha h\upsilon)^{1/2} = C(h\upsilon - E_g)$$

where, α is the absorption coefficient of the solid at a certain value of wavelength λ, h is Planck's constant, C is the proportionality constant, υ is the frequency of light, E_g is the band gap energy.

Fig. 2(b) shows the relationship of $(\alpha h\upsilon)^{1/2}$ vs photon energy ($h\upsilon = 1239/\lambda$) for TiO$_2$ and also the GO@TiO$_2$ nanocomposites. The band gap for bare TiO$_2$ is 3.20 eV, whereas the band gap of GO@TiO$_2$ nanocomposites are 3.06, 3.0, 2.89, 2.84 & 2.80 eV corresponding to *GO@TiO$_2$-A, GO@TiO$_2$-B, GO@TiO$_2$-C, GO@TiO$_2$-D & GO@TiO$_2$-E* respectively i.e. with increase GO content band gap decreases. This result supports the qualitative observation of a red shift in the absorption edge of GO@TiO$_2$ nanocomposites as compared to the bare TiO$_2$. GO contains many oxygen containing groups such as carboxyl, hydroxyl and epoxide which are covalently bonded to its layers surfaces. There is a possibility that some of the unpaired π

7

electrons of GO can bonded with the free electrons present on the surface of TiO_2 nanoparticles to form Ti-O-C structure, resulting in the shifting of valence band and reduction in the band gap.[30]

3.2   *X-ray diffractometry (XRD)*

The X-ray diffraction patterns for the GO and the $GO@TiO_2$ nanocomposites with different weight % of TiO_2 are shown in **Fig.3**. GO exhibits a strong diffraction peak at 2θ= 11.5° corresponding to the reflection plane (001) with an interlayer spacing of 7.43 Å due to the oxygen containing functional groups on the carbon sheets.[31] $GO@TiO_2$ nanocomposites with different weight percentage of GO exhibit similar XRD patterns. The characteristic XRD peaks of the $GO@TiO_2$ nanocomposites at 2θ values of 25.5, 38.1, 48.3, 54.2, 55.2, 62.9, 69.5, 70.3 & 75.4 can be indexed to (101), (004), (200), (105), (211), (204), (116), (220) & (107) crystal planes, which represents the pure anatase phase of TiO_2. The characteristic peaks are confirmed by the reported JCPDS.[32] Noticeably, no typical diffraction peak belonging to the GO is observed in the $GO@TiO_2$ nanocomposites. The reason can be attributed to the fact that regular stack of GO is disturbed by the intercalation of anatase TiO_2.[31,33] Thus, the XRD pattern of the $GO@TiO_2$ composites confirms the homogeneous distribution of anatse TiO_2 within the GO stacks. Furthermore, the existence of grapheme oxide in $GO@TiO_2$ nanocomposites can be clearly elucidated by Raman analysis.

3.3   *Raman Spectra*

Raman spectroscopy is a powerful tool to analyze the crystalline quality of the carbon and the defect mediated peaks. **Fig.4** shows the Raman spectrum of GO (inset graph in **Fig.4**) and $GO@TiO_2$ nanocomposite. In the Raman spectrum first order dominant vibrational modes, D band $1351cm^{-1}$ corresponds to the A_{1g} symmetry mode of sp3 carbon indicates about the order or disorder in the system[34] and G band $1599 cm^{-1}$ corresponds to the vibrational mode of sp2 carbon provides information about the doubly degenerate E2g mode of the Brillonium zone centre.[35] The second order vibrational bands, $2D_1$ & $2D_2$ arises at $2717.36cm^{-1}$ & $2928.62cm^{-1}$ respectively originates from a two phonon double resonance Raman process and provides information on the stacking order of graphene with number of layers and shows often a doublet with increasing number of graphene layers. Another overtone weak band $2D^{/}$ is observed at $3194.23cm^{-1}$.[36] The intensity of G band is stronger than D band. In plane crystallite size, L_a

can be calculated from the intensity ratio of the G band to the D band by using the formula, L_a= 4.4 (L_G/L_D). The obtained L_a value is 4.89,[37,38] from this it can be concluded that the sample contains highly disordered and randomly arranged graphene sheets. The shape of the 2D band is sensitive to the no of layers of graphene and chemical doping. When GO combines with TiO_2, the crystal structure of carbon changes obviously. There are four specific vibration modes are located at around 141 ($E_{(g1)}$), 391 ($B_{1g(1)}$), 514 ($A_{1g}+B_{1g(2)}$) & 634cm-1 ($Eg_{(2)}$) indicating the presence of the anatase phase of TiO_2 in the sample.[39]

3.4 *SEM Analysis & EDX*

The surface characteristics of the GO and the GO@TiO_2 nanocomposites are investigated with SEM analysis and the micrographs are shown in **Fig.5.** For the pure GO a flat multilayered structure with stacked GO sheets is observed at higher magnifications (Fig.5a) [40]. SEM micrographs (Fig.5c) shows that the flat layered structure of the GO is disappeared and a rough surface morphology is noticed for GO@TiO_2 nanocomposites. The change in morphology of the GO@TiO_2 nanocomposites can be attributed to the successful incorporation of TiO_2 into the GO sheets. The energy dispersive X-ray spectrum (EDX) of the GO sheets and GO@TiO_2 nanocomposites indicates the successful distribution of TiO_2 nanoparticles into the GO sheets (Fig.5b and 5d). The introduction of TiO_2 into the GO is confirmed from the elemental typical mapping images of titanium, oxygen and carbon.

3.5 *TEM Analysis*

Fig.6 represents the morphological image of synthesized GO and GO@TiO_2 nanocomposite from transmission electron microscopy. TEM micrographs of GO showed two dimensional layered and flat like structure with micrometers long wrinkles (**Fig.6a**). At higher magnification the TEM micrographs of GO show a completely amorphous and disordered structure (**Fig.6b**).[41] TEM micrographs of GO@TiO_2 nanocomposite, showed that large number of TiO_2 nanoparticles are densely deposited onto the GO sheets. The electron transfer processes in the solar cells are facilitated by the homogeneously and closely dispersed TiO_2 nanoparticles on the GO sheets **(Fig.6(c & d))**. The corresponding HRTEM image showed clear lattice fringes of TiO_2.

3.6 *The morphology of PVA gel electrolyte:*

The surface and cross sectional SEM images of PVA gel electrolyte are shown in Fig. 7 (a) and (b). A uniform surface with smooth outer morphology is observed in case of the surface view of the gel electrolyte. The cross sectional morphology of the chemically cross linked hydrogel images showed wavy surface. The surface morphology of the intact disc revealed some pores and dense areas in the inset.

3.7   *Electrochemical Impedance analysis of the PVA gel:*

In order to understand the electronic and ionic transport process in the DSSCs electrochemical impedance spectroscopy (EIS) is a very effective toll. We have carried out the EIS of the fabricated cells by exposing the cell to solar radiation of intensity AM1.5 G 100 mWcm^{-2}. The equivalent electrical circuit for the DSSCs, which is a combination of a series resistance and two time constant phase elements [42] is shown in Fig 8(a) and Fig 8(b) shows the Nyquist plot. Under exposer to light, the biased device shows a smaller arc in Nyquist plot at the higher frequency region corresponds to the capacitance resistance of the counter electrode / gel electrolyte interface (R_{ct1}) i.e. the charge transfer resistance at the Pt electrode/electrolyte interface. Another larger arc occurs at the mid frequency region which corresponds to the charge transfer process (R_{ct2}) at GO@TiO$_2$/dye/gel electrolyte and further charge transfer in the photoanode. [43] Another parameter at the high frequency intercept on the abscissa represents series resistance (R_s) which is associated with the electrolytes and electric contacts in the DSSCs. As shown in Table 2 it is observed that by changing the concentration of GO content in the photoanode, R_{ct1} remains almost same as we are using the same polymer gel electrolyte. But the R_{ct2} values are significantly increases with the increase in the weight% content of the GO in the photoanode than that of the pure TiO$_2$. This larger value of interfacial charge recombination resistance renders GO to increase the charge collection and transport of electrons at the interface of photoanode and the electrolyte. The charge transport mechanism becomes faster resulting in the reduction of electron recombination. [25] However, above a optimum GO loading (i.e. GO@TiO$_2$-D), it is observed that R_{ct2} value is low which may be due to the agglomeration of GO resulting in the creation of electron traps and also compete light harvesting with the dye molecules.

3.8   *Absorption spectroscopic investigation of dye adsorption*

UV-visible spectroscopy was used to study the effects of addition of GO to TiO_2 on the dye adsorption by the films. The absorption spectra of the N719 dye sensitized films of TiO_2 & GO@TiO_2 nanocomposites in the visible region are presented in Fig.9. The dye sensitized TiO_2 films shows absorption in the range of 400-800nm and the characteristic absorption of the N719 dye at around 530nm. The intensity of the absorption peak at 530nm increases with loading of GO in the nanocomposite of GO@TiO_2. Moreover, enhanced quantity of dye adsorption is indicative of enhanced surface area in the TiO_2 film. [44] The electron rich GO contains many oxygen containing groups like carboxyl on its surface and its addition to TiO_2 facilitating the anchoring of the N719 dye molecule. The obtained results suggest that the dye loading has increased in the order of GO content of TiO_2<GO@TiO_2-A<GO@TiO_2-E<GO@TiO_2-D. Absorbance measurements from Fig.9 indicate increased dye adsorption by about 40% in the case of GO@TiO_2-D nanocomposite film, and by 25 and 16% in the case of GO@TiO_2-E and GO@TiO_2-A nanocomposite film respectively. Upto an optimum concentration of GO a large amount of dye molecules are absorbed in the photoanode, leading to a strong light harvesting in the device. [45]

3.9   *Photovoltaic performance of the fabricated DSSCs devices*

GO@TiO_2 nanocomposites were employed as the photoanode material in the PVA gel electrolyte based quasi solid state DSSCs. The J-V curves and PV characteristics for DSSCs based on the different photoanode were evaluated under illumination of simulated solar light of 100mW cm^{-2} AM 1.5 and are exhibited in Table 3& Fig.10. The DSSCs prepared with GO@TiO_2-D nanocomposite as the photoanode exhibited the highest short circuit photocurrent density (J_{sc}) of 7.67mAcm^{-2} and the highest conversion efficiency of 3.97%. DSSCs obtained from the bare TiO_2 photoanode exhibits conversion efficiency of 0.99% and J_{sc} of 2.51mAcm^{-2}. However the photocurrent densities as well as the conversion efficiency increases with the addition of GO reaching a peak value and then declined with the higher concentration of GO in the GO@TiO_2 nanocomposite. Compared to the DSSCs with the bare TiO_2 nanoparticles photoanode, the conversion efficiency and J_{sc} of the DSSC with GO@TiO_2-D are significantly improved by 55% & 67% respectively. However, V_{oc} values remained fairly constant in the range of 0.65-0.75V. A small amount of GO in the photoanode is sufficient to enhance the electron injection and electron transfer rate in the DSSC operation thereby accelerating the charge transport mechanism. Subsequently, the electron recombination is reduced which extends

the electron lifetime in the photoanode. [25] In turn it can be said that, the introduced 2D GO bridges increases the formation of more conductive pathways to transport charge i.e. by decreasing the transport resistance and thus increases the photocurrent and suppress the electron in TiO_2 to recombine with the dye and redox species. It is observed that beyond the optimum amount of GO concentration, J_{sc} decreased which may be due to the decrease in the film transmittance hindering the electron transportation upon illumination. [46] The enhancement of the J_{sc} and FF was also attributed to the enhancement of the charge collection and transport of electron through different channels of gel electrolyte.

The long term stability of DSSCs assembled by using PVA polymer gel electrolyte was compared with that for a liquid electrolyte based cell and results are summarized in Fig.11 which compares the variation of PCE as a function of time. For this stability study, the devices were stored under dark at 65°C and 85% relative humidity. It is observed that PCE of the polymer gel electrolyte based devices is decreased by 5 %, whereas the PCE for liquid electrolyte based devices is decreased by about 19% after 800 h. In case of the liquid electrolyte based devices, leakage and evaporation of the solvent take place with time and also dye molecule start desorbing from the TiO_2 based photoanode. In case of the polymer gel electrolyte based devices, as the electrolyte is entrapped within the polymer matrix the evaporation as well as the leakage of the solvent from the cell is reduced.

4. Conclusion

The self assembled $GO@TiO_2$ hybrid nanocomposites have been used as photoanode in fabrication of DSSCs. XRD, UV-Visible and Raman spectroscopy confirm successful formation of the nanocomposite. The morphological analysis reveals the uniform formation of $GO@TiO_2$ nanocomposite. The EIS demonstrates that GO reduces the electron recombination and improving the electron transport through the film. The incorporation of GO into the TiO_2 results in the enhancement of device parameters Jsc, Voc and PCE. As the GO concentration increases from 0.25 to 2.5 wt%, the PCE increases from 1.37 to3.97 % due to the rapid charge transport mechanism in the photoanode. GO offers an improved rate of collection and transport of electrons. Moreover, upto an optimum concentration of GO a large amount of dye molecules are absorbed in the photoanode with higher concentration of GO thus leading to a strong light harvesting in the device.

REFERENCE

1. M. Grätzel, *Nature* , 2001, **414**, 338-344.
2. A. Hagfeldt, G. Boschloo, L. C. Sun, L. Kloo and H. Pettersson, *Chem. Rev.*, 2010, **110,** 6595-6663.
3. V. Galstyan, A. Vomiero, I. Concina, A. Braga, M. Brisotto, E. Bontempi, G. Faglia and G. Sberveglieri, *Small*, 2011, **7**, 2437-2442.
4. M. Law, L. E. Greene, J. C. Johnson, R. Saykally, P. D. Yang, *Nat. Mater.*, 2005, **4**, 455−459.
5. A. Vomiero, I. Concina, M. M. Natile, E. Comini, G. Faglia, M. Ferroni, I. Kholmanov and G. Sberveglieri, *Appl. Phys. Lett.*, 2009, **95**, 193104 (1-3).
6. N. Memarian, I. Concina, A. Braga, S. M. Rozati, A. Vomiero and G. Sberveglieri, *Angew. Chem. Int. Ed.*, 2011, **50**, 12321−12325.
7. J. van de Lagemaat, K. D. Benkstein and A. J. Frank, *J. Phys. Chem. B*, 2001, **105**, 12433−12436.
8. N. Kopidakis, N. R. Neale, K. Zhu, J. van de Lagemaat and A. Frank, *J. Appl. Phys. Lett.*, 2005, **87**, 202106.
9. A. Kongkanand, R. Martínez Domínguez and P. V. Kamat, *Nano Lett.*, 2007, **7**, 676−680.
10. A. Kongkanand and P. V. Kamat, *ACS Nano*, 2007, **1**, 13 −21.
11. J. van de Lagemaat, N. G. Park and A. J. Frank, *J. Phys. Chem. B*, 2000, **104**, 2044−2052.

12. H. Tian, L. Hu, C. Zhang, L. Mo, W. Li, J. Sheng, S. Dai, *J. Mater. Chem.*, 2012, **22**, 9123−9130.

13. F. Huang, Q. Li, G. J. Thorogood, Y. B. Cheng and R. A. Caruso, *J. Mater. Chem.*, 2012, **22**, 17128−17132.

14. J. Du, J. Qi, D. Wang and Z. Tang, *Energy Environ. Sci.*, 2012, **5**, 6914−6918.

15. T. Chen, G. H. Guai, C. Gong, W.Hu, J. Zhu, H. Yang, Q. Yan and C. M. Li, *Energy Environ. Sci.*, 2012, **5**, 6294−6298.

16. K. Kakiage, T. Tokutome, S. Iwamoto, T. Kyomen and M. Hanaya, *Chem. Commun.*, 2013**, 49**, 179−180.

17. J. Yan and F.Zhou, *J. Mater. Chem.*, 2011, **21**, 9406−9418.

18. G. K. Mor, K. Shankar, M. Paulose, O. K. Varghese and C. A. Grimes, *Nano Lett.*, 2005, **6**, 215−218.

19. Z. Liu and M. Misra, *ACS Nano*, 2010, **4**, 2196−2200.

20. Z. Sun, J. H.Kim, Y.Zhao, F. Bijarbooneh, V. Malgras and S. X. Dou, *J. Mater. Chem.*, 2012, **22**, 11711−11719.

21. J. Wang and Z. Lin, *Chem. Asian J.*, 2012, **7**, 2754−2762.

22. S. Muduli, W. Lee, V. Dhas, S. Mujawar, M. Dubey, K. Vijayamohanan, S. H. Han and S. Ogale, *ACS Appl. Mater. Interfaces,* 2009, **1**, 2030−2035.

23. J. Yu, J. Fan and B. Cheng, *J. Power Sources*, 2011, **196**, 7891−7898.

24. Y. H. Jang, X. Xin, M. Byun, Y. J. Jang, Z. Lin and D. H. Kim, *Nano Lett.*, 2011, **12**, 479−485.

25. N. Yang, J. Zhai, D. Wang, Y. Chen and L. Jiang, *ACS Nano*, 2010, **4**, 887–894 .

26. W. S. Hummers and R. E. Offeman, *J. Am. Chem. Soc.,* 1958, **80** , 1339.

27. D. H. Wang, D. W. Choi, J. Li, Z. G. Yang, Z. M. Nie, R. Kou, D. H. Hu, C. M. Wang, L. V. Saraf and J. G. Zhang, *ACS Nano*, 2009, **3**, 907–914.

28. H. S. Mansur, R. L. Oréfice and A. A. P. Mansur, *Polymer*, 2004, **45**, 7193–7202.

29. K. Dai, L. Lu, Q. Liu, G. Zhu, Q. Liua and Z. Liua, *Dalton Trans,* 2014, **43**, 2202–2210.

30. V. Štengl, S. Bakardjieva, T. M. Grygar, J. Bludská and M. Kormunda, *Chemistry Central Journal,* 2013**, 7**, 41.

31. P. G. Liu, K. C. Gong, P. Xiao and M. Xiao, *J. Mater. Chem.,* 2000, **10**, 933-935.

32. Y. W. Jun, M. F. Casula, J. H. Sim, S. Y. Kim, J. Cheon and A. P. Alivisatos, *J. Am. Chem. Soc.* 2003, **125**, 15981-15985.

33. C. Xu, X. D. Wu, J. W. Zhu and X. Wang, *Carbon*, 2008, **46**, 386-389.

34. M. S. Dresselhaus, A. Jorio, M. Hofmann, G. Dresselhaus and R. Saito, *Nano Lett.*, 2010, **10**, 751–758.

35. J. Lu, J. X. Yang, J. Wang, A. Lim, S. Wang and K. P. Loh, *ACS Nano,* 2009, **3**, 2367–2375.

36. A. C. Ferrari, J. C. Meyer, V. Scardaci, C. Casiraghi, M. Lazzeri, F. Mauri, S. Piscanec, D. Jiang, K. S. Novoselov, S. Roth and A. K. Geim, *Phys. Rev. Lett.*, 2006, **97**, 187401-187404.

37. M. A. Pimenta, G. Dresselhaus, M. S. Dresselhaus, L. A. Cancado, A. Jorio and R. Saito, *Phy. Chem. Chem. Phys.*, 2007, **9**, 1276-1290.

38. A. C. Ferrari, *Solid State Commun.,* 2007, **143**, 47-57.

39. Y. Lei, L. D. Zhang and J. C. Fan, *Chem. Phys. Lett.*, 2001, **338**, 231–236.

40. L. L. Zhang, S. Zhao, X. N. Tian, X. S. Zhao, *Langmuir,* 2010, **26**, 17624-17628.

41. G. X. Wang, J. Yang, J. Park, X. L. Gou, B. Wang, H. Liu and J. Yao, *J. Phys. Chem. C.,* 2008, **112**, 8192–8195.

42. F. F. Santiago, J. Bisquert, G. G. Belmonte, G. Boschloo and A. Hagfeldt, *Sol. Energy Mater. Sol. Cells,* 2005, **87,** 117-131.

43. M. Miyashita, K. Sunahara, T. Nishikawa, Y. Uemura, N. Koumura, K. Hara, A. Mori, T. Abe, E. Suzuki and S. Mori, *J. Am. Chem. Soc.*, 2008, **130,** 17874-17881.

44. L. Zhang and Z. S. Wang, *J. Mater. Chem. C*, 2016, **4**, 3614-3620.

45. H. Wang, B. Wang, J. Yu, Y. Hu, C. Xia, J. Zhang and R. Liu, *Sci. Rep.,*2014, **5**, 9305.

46. Y. B. Tang, C. S. Lee, J. Xu, Z. T. Liu, Z. H. Chen, Z. B. He, Y. L. Cao, G. D. Yuan, H. S. Song, L. M. Chen, L. B. Luo, H. M. Cheng, W. J. Zhang, I. Bello and S. T. Lee, *ACS Nano*, 2010, **4**, 3482-3488.

Legend to Tables

1. **Table1:** Composition for the synthesis of $GO@TiO_2$ nanocomposites.

2. **Table2:** Various parameters determined by EIS measurements of the $GO@TiO_2$ nanocomposites based photoanode and polymer gel electrolytes.

3. **Table3:** Photovoltaic characteristics of the DSSCs with the $GO@TiO_2$ nanocomposites based photoanode and polymer gel electrolytes

Legend to Figures

1. **Fig. 1:** Schematic presentation of the GO@TiO$_2$ nanocomposite based photoanode for quasi solid state DSSC

2. **Fig. 2: (a)** UV-vis absorption spectra for TiO$_2$ and GO@TiO$_2$ nanocomposites

   (b) Tauc's plot for optical band-gap calculation for TiO$_2$ and GO@TiO$_2$ nanocomposites

3. **Fig. 3:** XRD patterns for GO and GO@TiO$_2$ nanocomposites

4. **Fig. 4:** Raman Spectra for GO and GO@TiO$_2$-C nanocomposite

5. **Fig. 5:** SEM images of the (a) GO and (c) GO@TiO$_2$-D nanocomposite

   EDX-spectrum of the a) GO and (c) GO@TiO$_2$-D nanocomposite

6. **Fig. 6:** TEM micrographs of the GO (a,b) and GO@TiO$_2$-D nanocomposite (c,d)

7. **Fig. 7:** SEM images of the PVA a) surface view and b) cross sectional view

8. **Fig. 8: (a)** The equivalent electrical circuit for the fabricated DSSCs

   (b) EIS analysis spectra for all the nanocomposites based photoanode. (Inset) expansion of the first semicircle

9. **Fig. 9:** UV-visible absorption spectra N719 dye adsorbed on TiO$_2$ and GO@TiO$_2$ nanocomposites photoanode

10. **Fig. 10:** Photocurrent density versus voltage plots for all the devices fabricated with all the nanocomposites

11. **Fig. 11:** Stability graph of the fabricated device with GO@TiO$_2$-D photoanode (a) Liquid electrolyte and (b) PVA gel electrolyte

Table 1

$TiO_2@GO$	$GO@TiO_2$-A (0.25 wt%)	$GO@TiO_2$-B (0.5 wt%)	$GO@TiO_2$-C (1 wt%)	$GO@TiO_2$-D (2.5 wt%)	$GO@TiO_2$-E (5 wt%)
GO (ml)	1.85	3.70	7.40	18.50	37
SDS (ml)	0.11	0.22	0.44	1.10	2.20

Table 2

Sample	R_s (ohm)	R_{ct1} (ohm)	R_{ct2} (ohm)	σ (Scm^{-1})
TiO$_2$ only	0.4498	0.2111	5.8439	0.4446
GO@TiO$_2$-A	0.4126	0.2079	6.1645	0.4847
GO @TiO$_2$-B	0.3799	0.2110	6.4228	0.5265
GO@TiO$_2$-C	0.3394	0.2068	6.9929	0.5893
GO@TiO$_2$-D	0.3088	0.2111	7.4561	0.6477
GO @TiO$_2$-E	0.3231	0.2142	7.0843	0.619

Table 3

Sample	J_{sc} (mA/cm^2)	V_{oc}(V)	FF	PCE, η (%)
TiO$_2$ only	2.5072	0.6501	0.61	0.99
GO@TiO$_2$-A	3.2826	0.6547	0.63	1.37
GO@TiO$_2$-B	4.0317	0.6991	0.64	1.80
GO@TiO$_2$-C	4.7821	0.7073	0.65	2.20
GO@TiO$_2$-D	7.6654	0.7617	0.68	3.97
GO@TiO$_2$-E	6.6554	0.7097	0.67	3.16
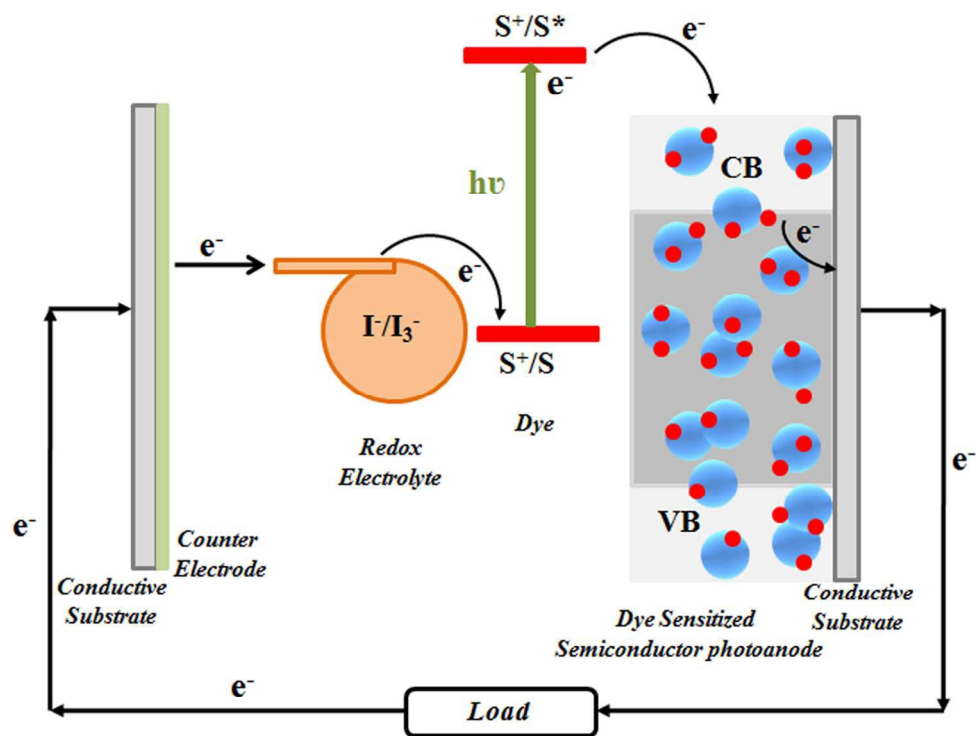
S⁺/S*

e⁻

e⁻

hυ

CB

e⁻

I⁻/I₃⁻

e⁻

S⁺/S

VB

e⁻

Dye

e⁻

Redox
Electrolyte

e⁻

Counter
Electrode

Conductive
Substrate

Conductive
Substrate

Dye Sensitized
Semiconductor photoanode

e⁻

e⁻

Load

Fig. 1

Schematic presentation of the GO@TiO2 nanocomposite based photoanode for quasi solid state DSSC
143x114mm (300 x 300 DPI)
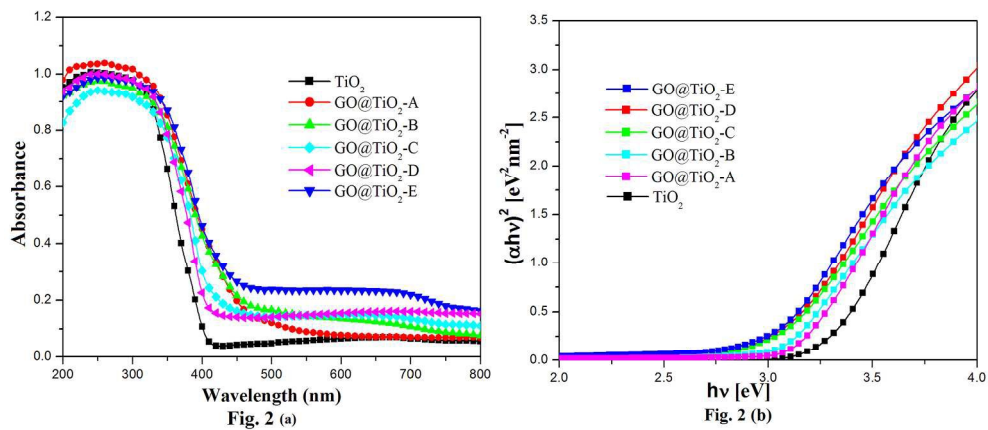
Fig. 2: (a) UV-vis absorption spectra for TiO2 and GO@TiO2 nanocomposites
(b) Tauc's plot for optical band-gap calculation for TiO2 and GO@TiO2 nanocomposites

715x307mm (200 x 200 DPI)
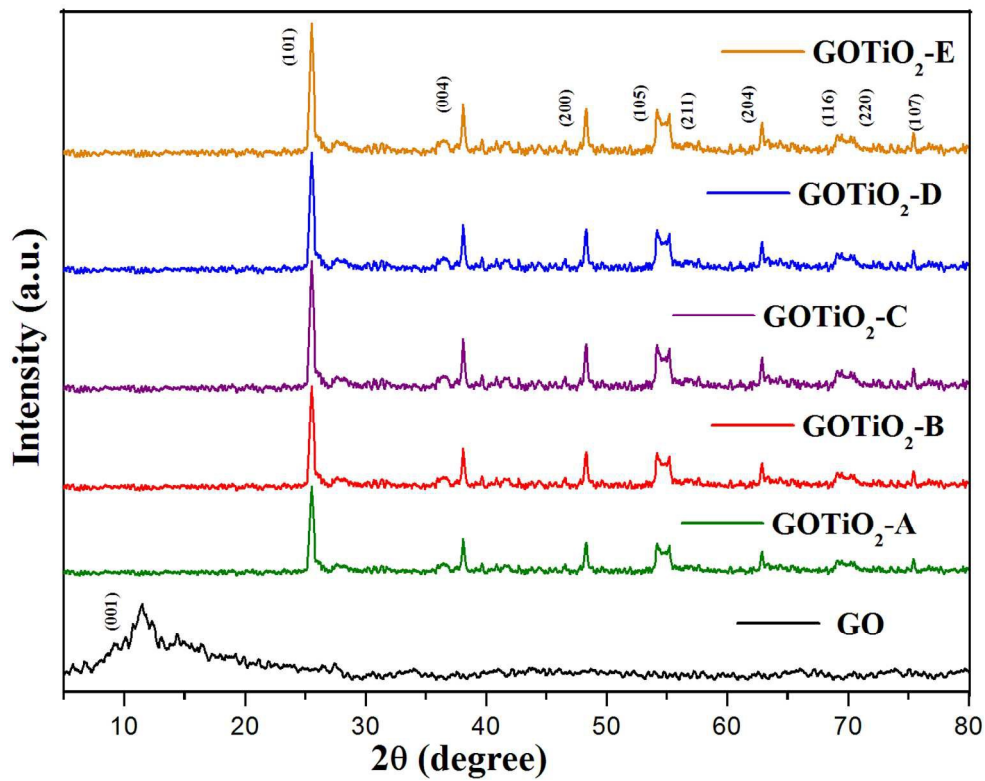
Fig. 3: XRD patterns for GO and GO@TiO2 nanocomposites
305x257mm (300 x 300 DPI)
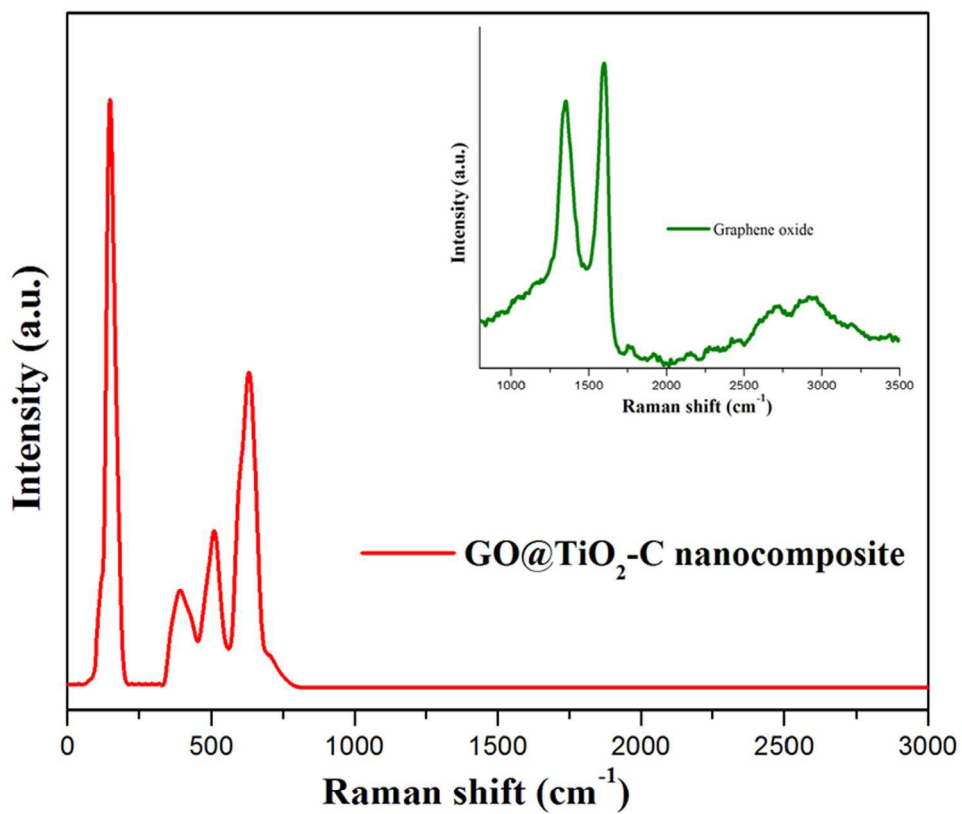
Fig. 4

Fig. 4: Raman Spectra for GO and GO@TiO2-C nanocomposite
197x178mm (300 x 300 DPI)

Element	Weight%	Atomic%
C K	54.47	61.44
O K	45.53	38.56
Totals	100.00	

Element	Weight%	Atomic%
C K	56.75	66.33
O K	35.92	31.52
Ti K	7.33	2.15
Totals	100.00	
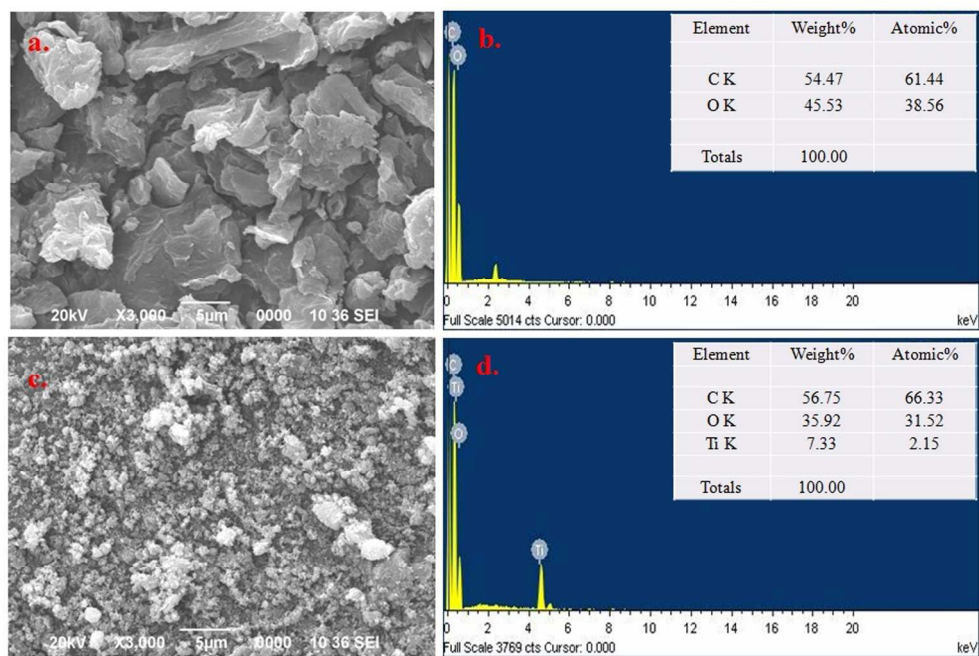
Fig. 5

Fig. 5: SEM images of the (a) GO and (c) GO@TiO2-D nanocomposite
EDX-spectrum of the a) GO and (c) GO@TiO2-D nanocomposite

245x187mm (300 x 300 DPI)
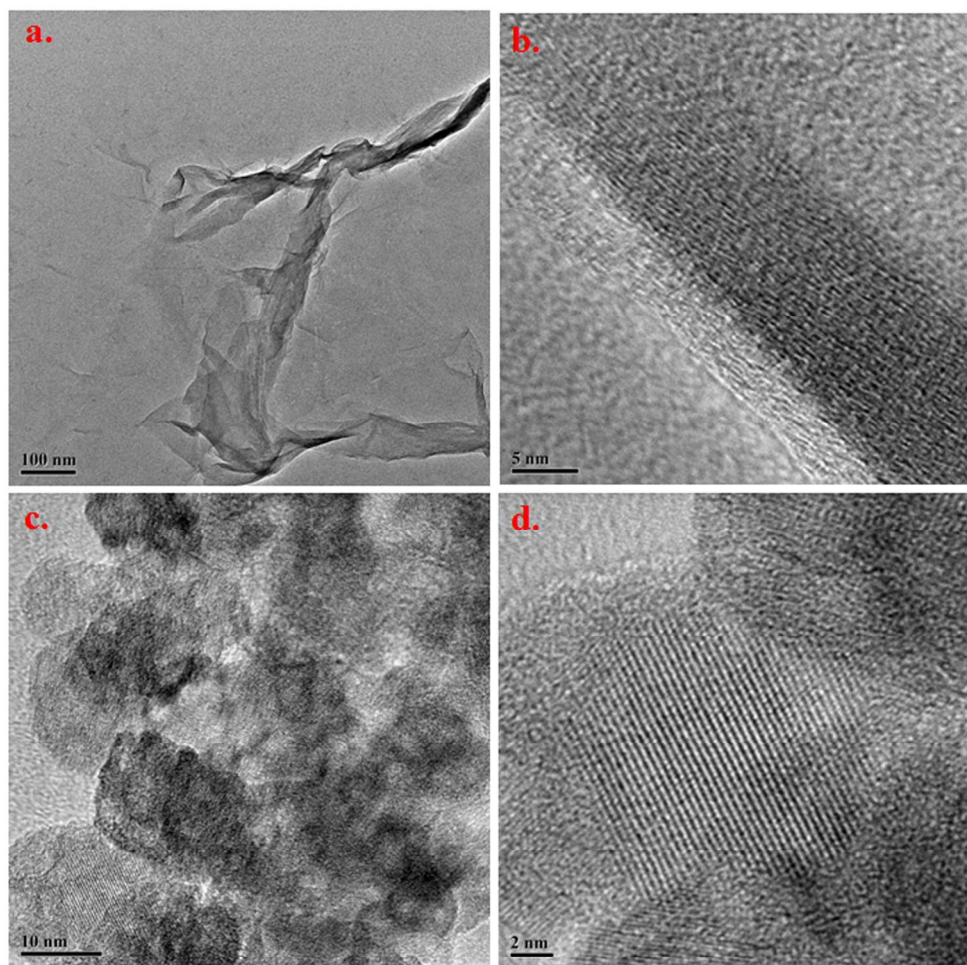
Fig. 6

Fig. 6: TEM micrographs of the GO (a,b) and GO@TiO2-D nanocomposite (c,d)
191x204mm (300 x 300 DPI)
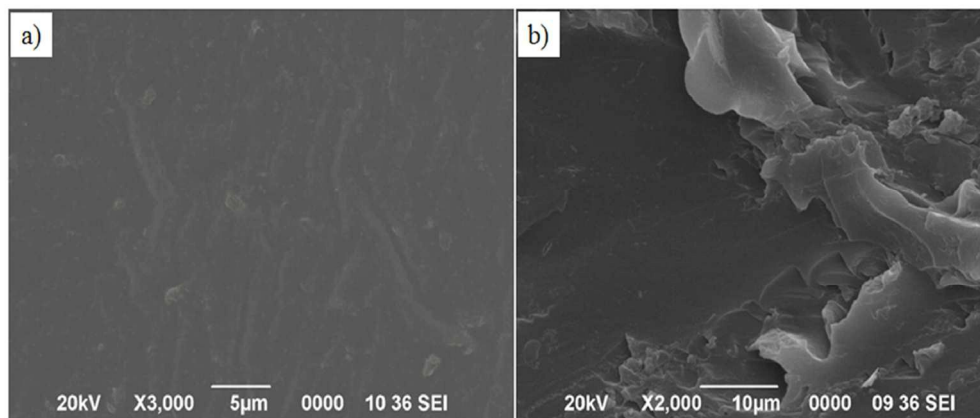
Fig. 7

Fig. 7: SEM images of the PVA a) surface view and b) cross sectional view
90x43mm (300 x 300 DPI)
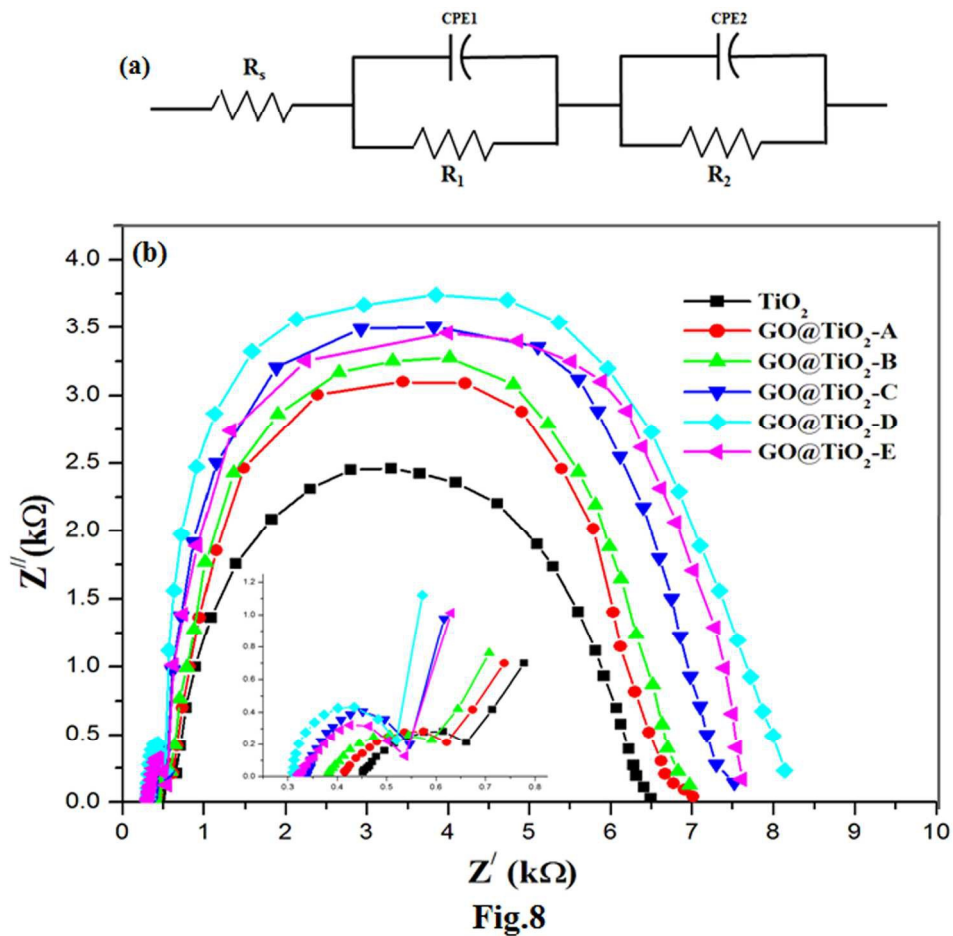
Fig. 8: (a) The equivalent electrical circuit for the fabricated DSSCs
(b) EIS analysis spectra for all the nanocomposites based photoanode. (Inset) expansion of the first semicircle

173x163mm (300 x 300 DPI)
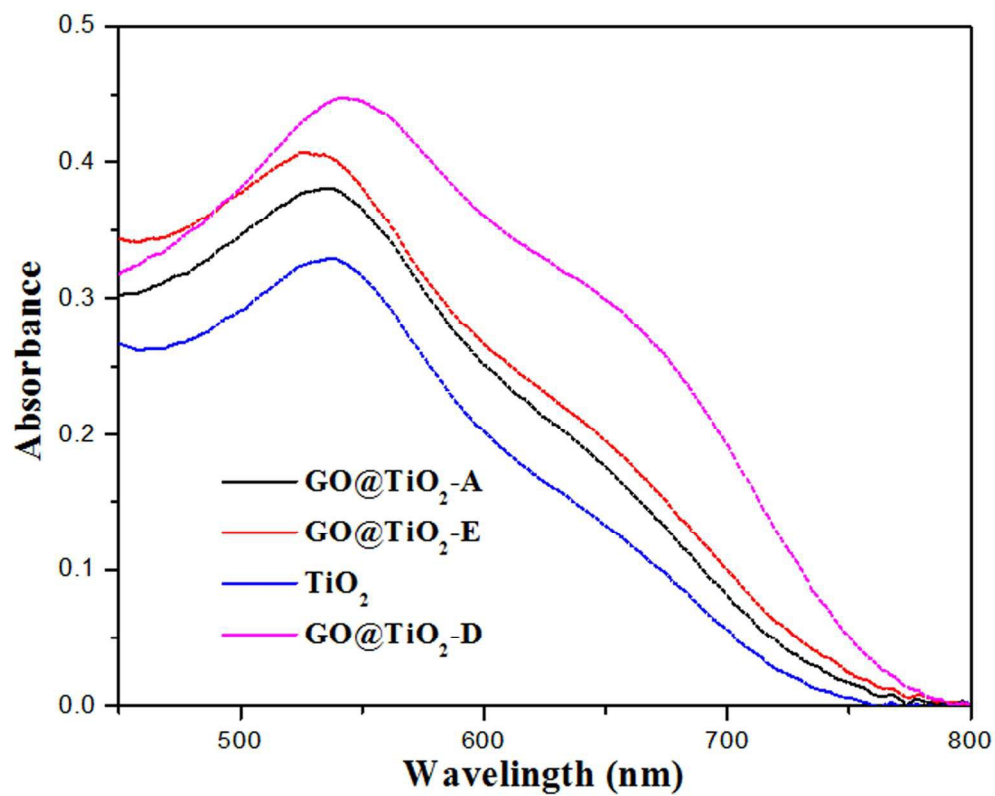
Fig. 9: UV-visible absorption spectra N719 dye adsorbed on TiO2 and GO@TiO2 nanocomposites photoanode

147x123mm (300 x 300 DPI)
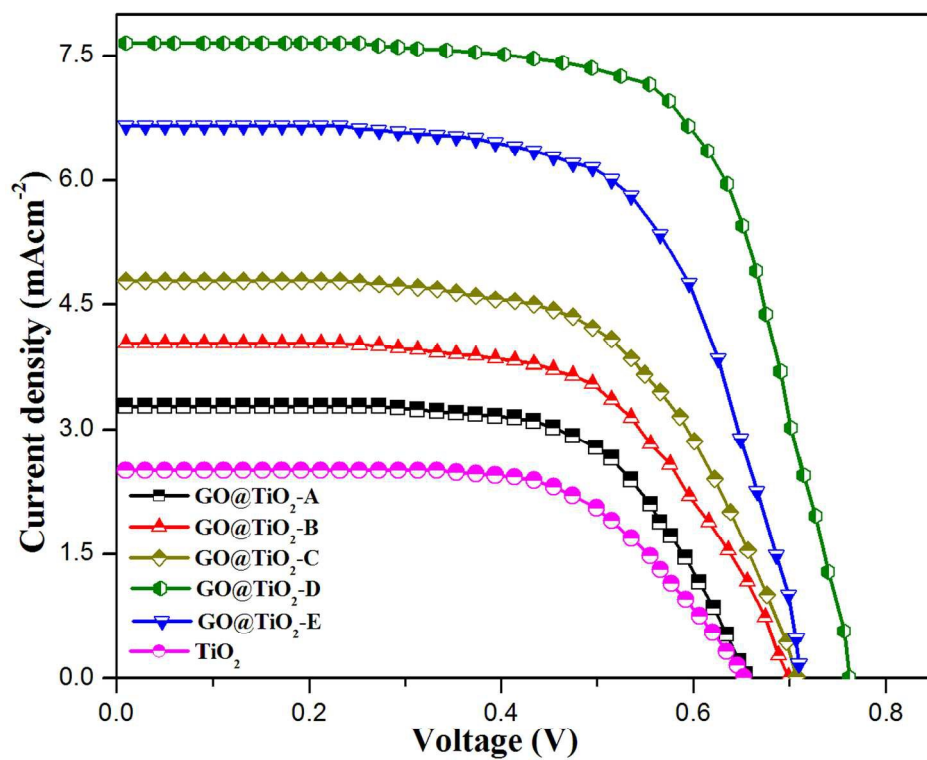
Fig. 10

Fig. 10: Photocurrent density versus voltage plots for all the devices fabricated with all the nanocomposites

201x173mm (300 x 300 DPI)
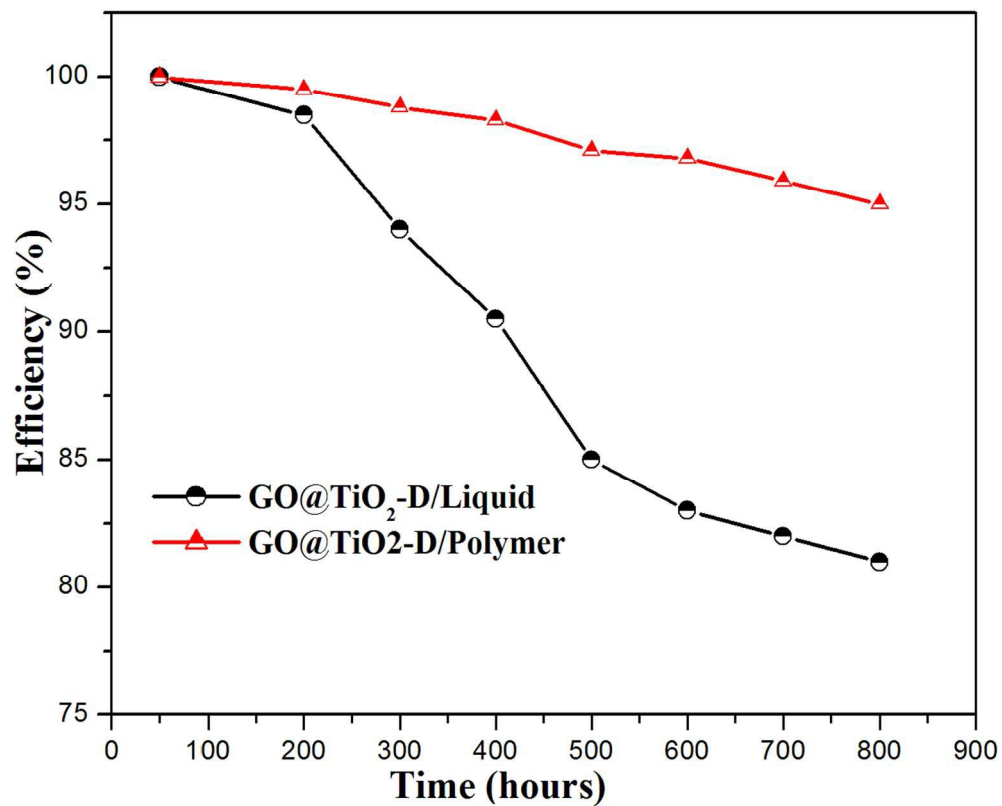
Fig. 11

Fig. 11: Stability graph of the fabricated device with GO@TiO2-D photoanode (a)
Liquid electrolyte and (b) PVA gel electrolyte

191x166mm (300 x 300 DPI)

133x74mm (300 x 300 DPI)